JWST observations of starbursts: cold clouds and plumes launching in the M 82 outflow

Fisher, D.B.; Bolatto, A.D.; Chisholm, J.; Fielding, D.; Levy, R.C.; Tarantino, E.; ... ; Klessen, R.S.

Monthly Notices of the ROYAL ASTRONOMICAL SOCIETY

MNRAS **538,** 3068–3083 (2025) https://doi.org/10.1093/mnras/staf363
Advance Access publication 2025 March 3

JWST observations of starbursts: cold clouds and plumes launching in the M 82 outflow

Deanne B. Fisher [1,2★] Alberto D. Bolatto,[3,4] John Chisholm [5] Drummond Fielding [6,7] Rebecca C. Levy [8,9†] Elizabeth Tarantino,[9] Martha L. Boyer,[9] Serena A. Cronin,[3] Laura A. Lopez,[10,11] J. D. Smith [12] Danielle A. Berg,[5] Sebastian Lopez,[10,11] Sylvain Veilleux,[3,4] Paul P. van der Werf,[13] Torsten Böker [14] Leindert A. Boogaard [15] Laura Lenkić,[16] Simon C. O. Glover [17] Vicente Villanueva,[18] Divakara Mayya [19] Thomas S.-Y. Lai,[20] Daniel A. Dale,[21] Kimberly L. Emig,[22,23] Fabian Walter,[15] Monica Relaño [24] Ilse De Looze [25] Elisabeth A. C. Mills,[26] Adam K. Leroy,[10] David S. Meier,[27,28] Rodrigo Herrera-Camus[18,29] and Ralf S. Klessen [17,30]

Affiliations are listed at the end of the paper

Accepted 2025 February 11. Received 2025 February 5; in original form 2024 May 8

ABSTRACT

In this paper, we study the filamentary substructure of 3.3 μm polycyclic aromatic hydrocarbon (PAH) emission from *JWST*/NIRCam observations in the base of the M 82 star-burst driven wind. We identify plume-like substructure within the PAH emission with widths of ∼50 pc. Several of those plumes extend to the edge of the field-of-view, and thus are at least 200–300 pc in length. In this region of the outflow, the vast majority (∼70 per cent) of PAH emission is associated with the plumes. We show that those structures contain smaller scale 'clouds' with widths that are ∼5–15 pc, and they are morphologically similar to the results of 'cloud-crushing' simulations. We estimate the cloud-crushing time-scales of ∼0.5–3 Myr, depending on assumptions. We show this time-scale is consistent with a picture in which these observed PAH clouds survived break-out from the disc rather than being destroyed by the hot wind. The PAH emission in both the mid-plane and the outflow is shown to tightly correlate with that of Pa α emission (from *Hubble Space Telescope* data), at the scale of both plumes and clouds, though the ratio of PAH-to-Pa α increases at further distances from the mid-plane. Finally, we show that the outflow PAH emission reaches a local minimum in regions of the M 82 wind that are bright in X-ray emission. Our results are consistent cold gas in galactic outflows being launched via hierarchically structured plumes, and those small scale clouds are more likely to survive the wind environment when collected into the larger plume structure.

Key words: galaxies: evolution – galaxies: starburst.

1 INTRODUCTION

Large scale galactic winds contribute to the enrichment of the circumgalactic medium and play critical roles in regulating star formation by removing gas from the star-forming mid-plane of galaxies (Chevalier & Clegg 1985; Heckman, Armus & Miley 1990; Veilleux, Cecil & Bland-Hawthorn 2005; Tumlinson, Peeples & Werk 2017; Rupke 2018; Veilleux et al. 2020). This process is frequently invoked in models of galaxy evolution as a necessary component to match basic properties of galaxies, such as the stellar mass function and star formation rates in galaxies across cosmic history (Hopkins, Quataert & Murray 2012; Pillepich et al. 2018). Indeed, it is a consensus view in modern theories of galaxy evolution that winds driven by stellar feedback are a required component (for a review see Naab & Ostriker 2017).

Stellar feedback driven winds are launched from small-scale regions within the disc and are observed to extend many kiloparsecs above the plane. The wind is composed of a hot (10^6 K), highly ionized gas (Strickland & Heckman 2009) which is surrounded by a cone of warm (10^4 K) ionized material (Shopbell & Bland-Hawthorn 1998), and further out by cold gas (Walter, Weiss & Scoville 2002; Bolatto et al. 2013b; Leroy et al. 2015; Martini et al. 2018). The complexity of galactic winds lies in both the wide range of phases and the large dynamic range in spatial scales that play roles in shaping the kinematics and evolution of the gas (e.g. Fielding & Bryan 2022). Multiphase, resolved studies of outflows are direly needed but are observationally challenging.

An extra layer of complexity in understanding winds comes from observations over the past decade (Chisholm et al. 2015; Heckman et al. 2015; McQuinn, van Zee & Skillman 2019; Marasco et al. 2023) that consistently show that very little of the gas in winds

★ E-mail: dfisher@swin.edu.au
† NSF Astronomy and Astrophysics Postdoctoral Fellow.

escapes from the virial radius of the halo. It then follows that gas in wind re-accretes on to the disc in a so-called 'galactic fountain' scenario (Shapiro & Field 1976; Fraternali 2017). Winds therefore play a regulatory role, keeping the gas out of the disc for a period of time before it later becomes available for future star formation. The time-scales for this process are not well-known. Characterizing the energetics, evolution, and substructure of the galactic winds in detail is thus critical, as these properties will determine the amount of time for which the gas is outside of the galaxy as well as how the redistribution of baryons will ultimately shape galaxy growth.

The cold phase of galactic winds is the dominant mass component of gas that exists above the plane of the disc (Veilleux et al. 2020). Bolatto, Wolfire & Leroy (2013a) used early Atacama Large Millimeter Array (ALMA) observations to make resolved observations of the wind in NGC 253. They found gas connected to the hot X-ray wind and extends ∼300–500 pc, with a significant mass-loading of $\dot{M}_{\rm out}/{\rm SFR} \sim 10$–15. Similar results were found for M 82 (Leroy et al. 2015; Martini et al. 2018). Krieger et al. (2021) used high resolution (∼1 arcsec) observations of M 82 to find CO-bright clouds of gas extending over a kiloparsec from the mid-plane of the galaxy.

Theoretically explaining how the hot winds accelerate cold gas sufficiently to survive breakout from the disc, without destroying the cold clouds, has historically been challenging (Klein, McKee & Colella 1994; Scannapieco & Brüggen 2015; Schneider & Robertson 2017). Yet recent work in idealised 'cloud-crushing' or 'wind-tunnel' simulations has shown that the addition of cooling in the physics of the gas can play a critical role in cloud survival (Armillotta et al. 2017; Gronke & Oh 2018). In these simulations a cold ($T < 10^4$ K) overdensity of gas is placed in a hot ($T\sim 10^6$ K) wind fluid. Subsequent theoretical work argues that cloud size is a key parameter for the survivability of cold gas (Gronke & Oh 2020; Sparre, Pfrommer & Ehlert 2020; Abruzzo, Bryan & Fielding 2022; Farber & Gronke 2022). However, these results are highly dependent on the physics used in each simulation. Recent semi-analytic theory argues that the relationship between the cold clouds and hot phases may be critical to determining the energetic properties and evolution of winds (Fielding & Bryan 2022). It is therefore necessary to determine if the substructure of cold gas predicted in simulations is comparable to that of observed galactic winds. However, observing such clouds directly requires very high spatial resolution on the cold phase gas.

M 82 is arguably the best-studied galactic wind in the literature. This is due to both its proximity ($D = 3.6$ Mpc) and its orientation on the sky. M 82 is very near to edge-on (inclination ∼80°), which has allowed for the two nebulae extending outward from the stellar mid-plane of the galaxy to be easily observed (Lynds & Sandage 1963). It has, therefore, been well studied in cold (e.g. Walter et al. 2002; Engelbracht et al. 2006; Chisholm & Matsushita 2016; Martini et al. 2018; Krieger et al. 2021; Levy et al. 2023), warm (e.g. Shopbell & Bland-Hawthorn 1998), and hot gas phases (e.g. Strickland & Heckman 2009; Lopez et al. 2020).

In this work, we will focus on new observations from the *JWST* of the polycyclic aromatic hydrocarbon (PAH) emission at the centre of M 82. The data set is presented in Bolatto et al. (2024). PAH emission traces relatively cold gas (∼10^3 K) compared to the hot and warm-hot wind fluid in outflows. Engelbracht et al. (2006) showed, using observations from the *Spitzer Space Telescope*, that the PAHs in M 82 extend well outside the galaxy and are bright in the superwind. The PAH emission has filamentary sub-structure, which Leroy et al. (2015) show is in good agreement with the CO emission at large radii. This suggests that PAHs may be a good tracer of cold gas in outflows. High spatial resolution observations of cold gas in outflows have historically been difficult, as observations of CO or H I require interferometers. These observations are hampered by the ability to recover diffuse emission and surface brightness sensitivity. The availability of PAH and dust emission traced by *JWST* opens a new window into observing the cold component of outflows at high spatial resolution (∼1–10 pc in the nearest starburst galaxies).

In this paper, we adopt a distance of 3.6 Mpc (Freedman et al. 1994), such that 1 arcsec corresponds to 17.5 pc.

2 METHODS

2.1 *JWST* NIRCam images

In this paper, we focus on the NIRCam F335M image as a tracer of PAH emission in the centre of M 82. We also use F250M and F360M images to quantify the continuum level within the F335M filter. These dithered images have short exposures to avoid saturation in the bright central region of M 82. The observations are part of the *JWST* Cycle 1 GO programme #1701 (PI: Bolatto), which images the outflows in M 82 and NGC 253 (see Bolatto et al. 2024). The paper describes reduction of the images in more detail, and is summarized here for completeness.

The NIRCam data used in this paper were taken in October 2022, and cover only the centre of M 82.[1] We used a single SUB640 subarray observation with the RAPID readout, four intramodulebox primary dithers and four small-grid-dither subpixel dithers with six groups/integration.

The F335M targets the PAH feature at 3.3 μm. An advantage of analysing the shortest wavelength PAH feature at 3.3 μm is that it can be observed with higher spatial resolution than other transitions observed with at longer wavelength. For M 82, we can use the F335M flux as a means of tracing the morphology of the PAH emission, and thus the colder (∼10^2–10^3 K) gas in the outflow, at parsec scales. Draine et al. (2021) show that the 3.3 μm feature is very sensitive to smaller grain size and lower ionization states. The 3.3 μm flux can be affected by ionization and grain size, and the conversion to PAH mass is not well known in winds. We, therefore, do not use 3.3 μm flux alone as a dust mass tracer in this work. It is unclear how 3.3 μm flux will behave in the unique environment at the base of the outflow, outside the disc but still near to the starburst. Future work by our team will investigate the PAH flux ratios in the outflows of M 82 and NGC 253.

We processed the NIRCam uncalibrated data products with the *JWST* pipeline version 1.9.6 (Bushouse et al. 2023) and CRDS context JWST_1077.PMAP. We employed all the default parameters for Stage 2 processing. We used the *JWST*/*HST* Alignment Tool (JHAT; Rest et al. 2023) to align the individual exposures. First, we aligned the F250M exposures to the stars available in *Gaia*-DR3 using JHAT. Then, we created a catalogue of the stars from the F250M image by selecting pixels with brightness between 1 and 250 MJy sr^{-1}. These stars are used to align the other frames. We applied the Stage 3 step in the pipeline to the aligned files with the `tweakreg` step turned off, which yielded the final mosaics used in this work. We convolved the F335M and F250M images to match the point-spread function (PSF) of the F360M. This results in a PSF of our PAH image of 0.118 arcsec. We oversample the image to a pixel scale of 0.008 arcsec, which is finer than the original pixel scale. The resulting field-of-view is 46.6×46.6 arcsec^2.

[1]Automatic pipeline processed MAST mosaics can be found under http://dx.doi.org/10.17909/cwtn-nh63.

Extracting the PAH flux from the F335M image requires removal of underlying continuum. Ideally, this is carried out using continuum bands that bracket the emission feature. In our case, we have F250M and F360M images. However, Lai et al. (2020) show that the broad wing of the PAH emission feature can be significant in star-forming environments and partially falls in the F360M bandpass. As described in Bolatto et al. (2024), we follow a similar procedure as others (e.g. Sandstrom et al. 2023) in which we scale emission from the F335M filter to remove PAH and aliphatic contributions from the F360M filter.

It is very difficult to estimate a variance in the continuum subtracted image, as there are no regions without flux. We measure the standard deviation in several small (radius 0.1 arcsec) regions near the edge of the field-of-view that appear to not have significant sub-structure. We find values of ∼0.2–0.4 MJy sr^{-1}, which we can take as an upper-bound estimate on the flux density uncertainty in the image. We note this is very similar to the expected uncertainty of ∼0.25 MJy sr^{-1} from the *JWST* ETC.

2.2 NICMOS F187N

To measure ionized hydrogen emission, we use the *HST* NICMOS F187N and F160W for continuum subtraction. The data were taken as part of PID:7919 (PI: Sparks). The data from the programme are described in Böker et al. (1999). Alonso-Herrero et al. (2003) presents an analysis of NIC2 observations of M 82. These have finer spatial resolution but do not have the field of view that would allow us to maximize overlap with the NIRCam data. We therefore opt for the NIC3 observations.

The images were taken 1998 July 15 using NIC3 camera with the MULTIACCUM-STEP64 readout. The F187N image has an exposure time of 959 s and F160W has an exposure time of 191 s. The NIC3 observations cover a sufficient field of view to roughly match the NIRCam observations in this paper. NIC3 has lower angular resolution than our *JWST* data, with full width at half-maximum (FWHM) of order ∼0.3 arcsec.

We carry out continuum subtraction using the F160W continuum filter. We follow a similar procedure as outlined in Böker et al. (1999), in which the flux in F160W is scaled to the flux of F187N. The flux in F187N will be a combination of Paschen α emission and stellar continuum, and we therefore must find an appropriate scaling factor to subtract the continuum. For a given F160W flux there is a well-defined minimum of the F187N flux. The pixels with values near the minimum F187N/F160W are assumed to indicate the scaling between the continuum. The pixels with larger F187N/F160W are those more dominated by Paschen α emission. We aligned the F187N and F160W images using the world coordinate system of the images, and found sources to be aligned well. We fit a linear correlation between F187N and F160W ($\mathrm{F187N_{cont}} = a \times \mathrm{F160W} + b$) for only those pixels in the lowest 0.5 per cent of F187N/F160W. We ensure that this captures a range of flux values, and then subtract $\mathrm{F187N_{cont}}$ from the F187N image. It is difficult to estimate the flux after continuum subtraction is complete as emission likely fills the frame. To do this we take the median flux in regions far from any sub-structure in emission, which corresponds to $\sim 1.5 \times 10^{-20}$ erg s^{-1} Å^{-1} cm^{-2}. The final image is oversampled to a pixel scale of 0.063 arcsec and has a field-of-view of 46×46 arcsec^2.

Image registration with the NICMOS data requires an extra step, due to an offset in the WCS of the NICMOS data compared to the *JWST* NIRCam data. There were an insufficient number of point sources spread across the image for automated detection methods, as the mid-plane of the galaxy is blended at NICMOS resolution. We therefore identified 20 matching stars in the image, by-eye and then used centroid calculations to generate shifts for the WCS of the NICMOS continuum image to minimize the offset to the F250M image. We found the shift to be ∼0.96 arcsec in RA and ∼0.5 arcsec in DEC. We then applied the same offsets to the F187N image. We note that there were not enough point sources at large distance perpendicular to the mid-plane of M 82 to carry out any higher order corrections to match the images. However, the distortion corrections in NICMOS multidrizzle are very well characterized and we assume this correction, after using standard pipeline methods, is minimal. The final NICMOS image is offset from the NIRCam image, and leaves a region of ∼5 arcsec on the western and southern side of the image that is covered by NIRCam but not by NICMOS. This reduces the area of comparison slightly, but does not impact our results significantly.

2.3 NOEMA CO(1–0)

We use the CO(1–0) moment 0 map reported in Krieger et al. (2021) and refer readers to the original publication for more details. Krieger et al. (2021) produced a map that covers ∼7 arcmin on the major-axis and ±2.8 arcmin on the minor axis. This area is much larger than that of our current *JWST* data, but will be well matched to our upcoming wide-scale observations of M 82 with NIRCam and MIRI. The resulting CO(1–0) data cube has a median root-mean-square noise in a 5 km s^{-1} channel of 138 mK (or 5.15 mJy beam^{-1}) and spatial resolution of ∼1.9 arcsec.

2.4 *Chandra* X-ray data

We use data from Lopez et al. (2020) to characterize the X-ray emission in M 82, and refer to their paper for further details on the observations and data reduction. In short, Lopez et al. (2020) combine ACIS-S observations into an equivalent exposure time of 544 ks producing a broad-band X-ray image (0.5–7.0 keV). The X-ray images are point sources are removed. The FWHM of the on-axis PSF of *Chandra* is ∼0.492 arcsec. As discussed by the authors, the resulting map shows a diffuse halo that is in broad agreement with the generally known morphology of the M 82 wind. In our work, we will only use their map to study the location of X-ray peaks in relation to the cold gas tracer PAH.

3 PAH PLUMES EXTENDING FROM M 82 MID-PLANE

In Fig. 1, we reproduce three-colour images of M 82 from NIRCam observations. Bolatto et al. (2024) present the overall NIRCam data set, and include a qualitative discussion of the filamentary substructure in M 82, which we will study in more detail in this work. In Fig. 2, we compare the coverage of the NIRCam observations to the NICMOS and X-ray images used in this work.

Using our assumed distance of 3.6 Mpc the spatial resolution of the F335M is of order ∼1.8 pc. The position angle of the NIRCam image is such that the major-axis of the disc crosses the diagonal of the image. We therefore cover a range of distances for the structures extending vertically from the plane of the galaxy. For the outer structures the NIRCam image covers ∼250 pc from the disc, and in the centre this extends to ∼550–600 pc. PAH emission has been observed to distances of ±6 kpc from the disc (Engelbracht et al. 2006; McCormick, Veilleux & Rupke 2013). Our image in Fig. 1, therefore, represents the inner 5–10 per cent of the cold outflow. In

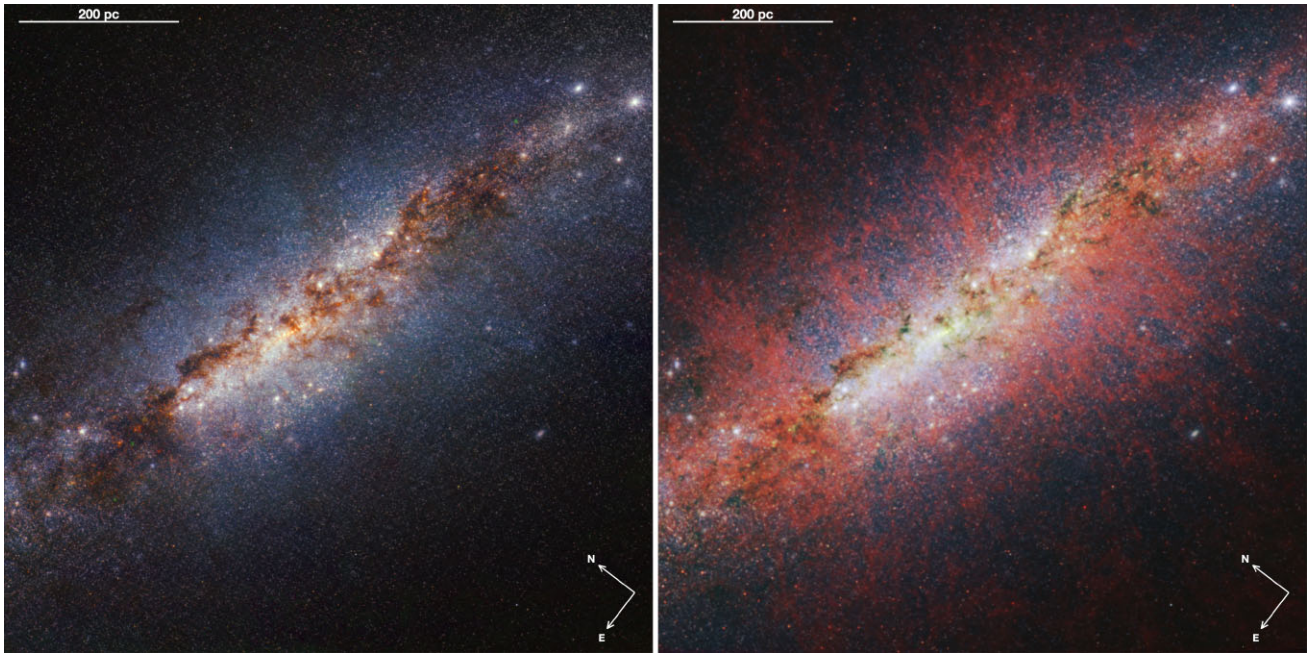

Figure 1. M 82 NIRCam observations, reproduced from Bolatto et al. (2024). The left panel shows a combination of F212N, F164N, and F140M for red, green, and blue, respectively. The right panel shows F335M, F250M, and F164N for red, green, and blue, respectively. The most significant difference in the two images comes from F335M filter, which is dominated by the PAH emission. There are clear filaments of PAH extending out of the mid-plane of the galaxy and connecting to the larger scale wind.

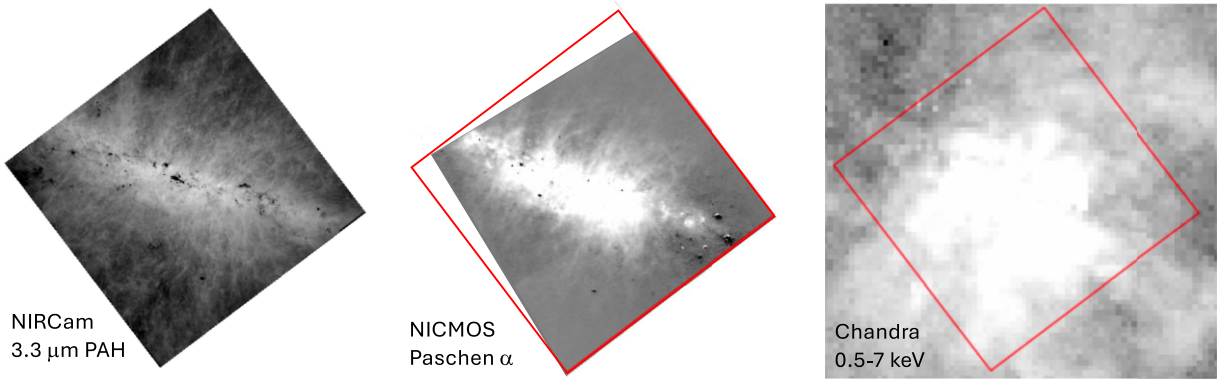

Figure 2. Images and field-of-view coverage of data sets used from this paper are shown. The images are 3.3 μm continuum removed PAH (left), continuum removed Paschen α from *HST*/NICMOS (middle) and 0.5–7 keV from *Chandra* (right). The NIRCam field-of-view for this paper is shown as a red rectangle in the right two images. The PAH extends to the edge of the field and likewise the X-ray goes far beyond the images. As described in Bolatto et al. (2024) the filamentary structure in both Paschen α and PAH is similar in morphology and position.

Fig. 2, the PAH clearly extends to the edge of the NIRCam field of view.

Overall, we identify a significant amount of filamentary gas plumes that are elongated away from the disc. We define a 'plume' as a coherent peak in the flux extending roughly perpendicular from the plane of the disc. Bolatto et al. (2024) identify several large (∼100 pc) overdensities of PAH emission. These are similar to the structures identified by Wills et al. (1999) in their VLA radio continuum observations, which is likewise shown with updated radio continuum in Bolatto et al. (2024). On the north side of the image (upper half in Figs 1 and 3) the four peaks in the normalized brightness slice are associated to plumes that are spaced at intervals of ∼100–150 from each other and extend outward to the edge of the field. These plumes extend and connect to the PAH emission structures observed at larger distances (Engelbracht et al. 2006; McCormick et al. 2013).

The southern outflow of M 82 also has filamentary structure. It is not as equally spaced. We note there are known differences in the mass loading and substructure of northern and southern outflows (Walter et al. 2002; Leroy et al. 2015; Chisholm & Matsushita 2016) and they have for many years been known to be asymmetric (Shopbell & Bland-Hawthorn 1998).

In Figs 3 and 4, we plot normalized brightness profiles of the PAH, CO, and Pa α emission in the regions $z = 80$ pc and 180 pc (on the north side, and corresponding negative values on the south side). We also show the PAH image for comparison. We note that the brightness profile is summed within the region and therefore favours values that are closer to the galaxy. This should be taken into account

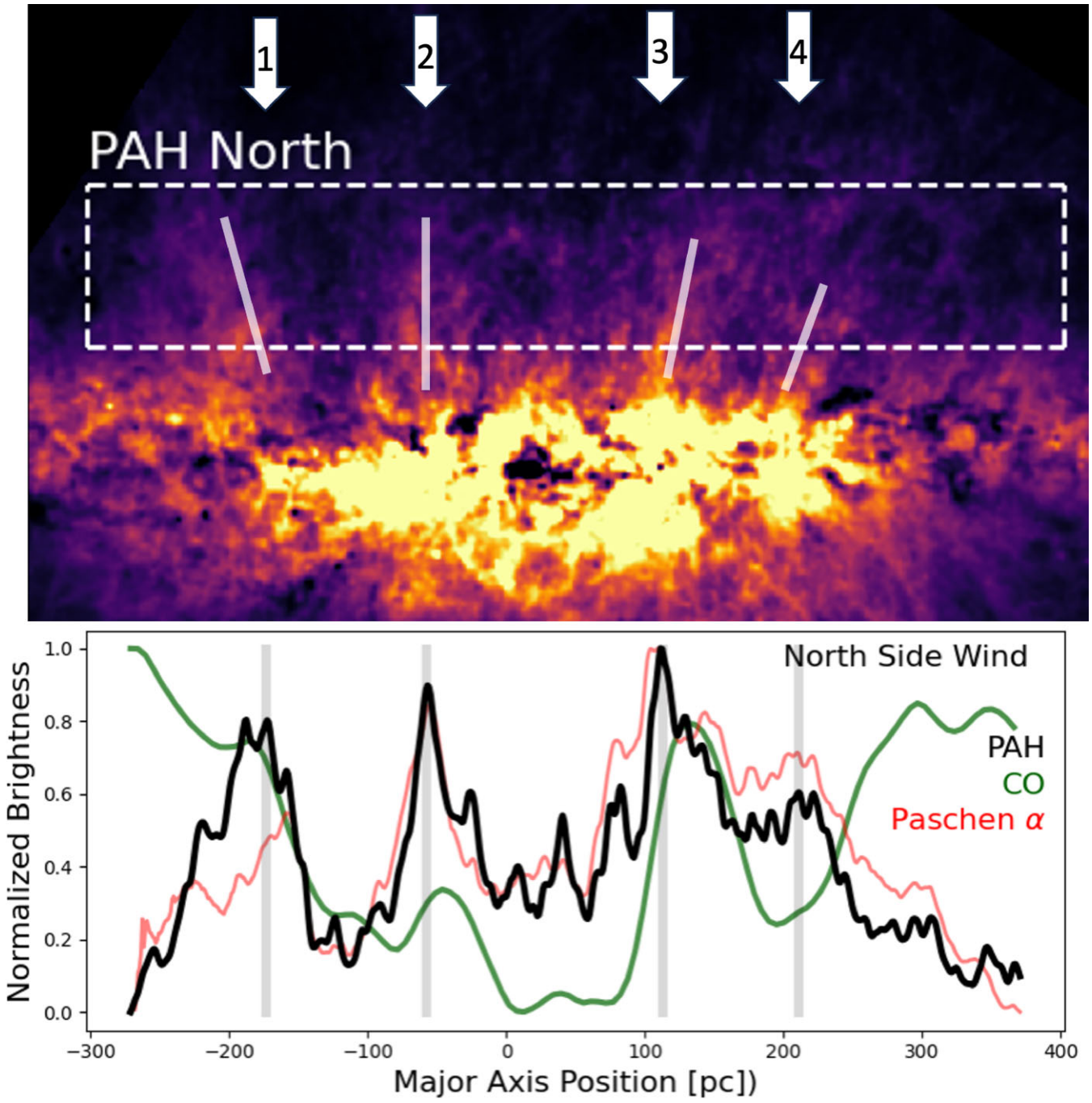

Figure 3. The *top panel* shows the PAH image. The white dashed rectangle represents the region analysed in the bottom panel of this figure. The solid lines indicate the positions of plumes. This line is not used in analysis and is only provided to guide the eye. The arrows show the position based on the horizontal cut, which will be weighted toward the brighter part of the plume, closer to the galaxy. The *bottom panel* shows horizontal slices of normalized flux for PAH (black), Pa α (red), and CO moment 0 (green). We normalize the flux such that the highest value in the slice is unity and the lowest value in the slice is zero. The aim of these diagrams is to identify the location of peaks in PAH. These are shown as vertical grey lines and numbered arrows in top panel.

when comparing the image to the galaxy. We tested use of median values in the same region, and this only slightly changes the location of peaks in the brightness profile. Overall the location of each peak in the brightness profile will change based on the position at which it is measured, and should be considered as only an approximate quantity.

We identify the locations of PAH emission peaks as arrows in the image and grey stripes in the panels below. The panels show horizontal slices of flux of the PAH emission that are centred $\sim$135 $\pm$ 50 pc above the mid-plane. The centre of the mid-plane is defined by the peak in the NIRCam F250W image of stellar continuum. This height is chosen to be beyond the 50 per cent height of the starlight, but still having good coverage within the image. The flux is normalized such that the peak value in each slice is unity and the minimum value in each slice is zero. The intention is to determine if the locations of the plumes in Fig. 1 are consistent with true peaks

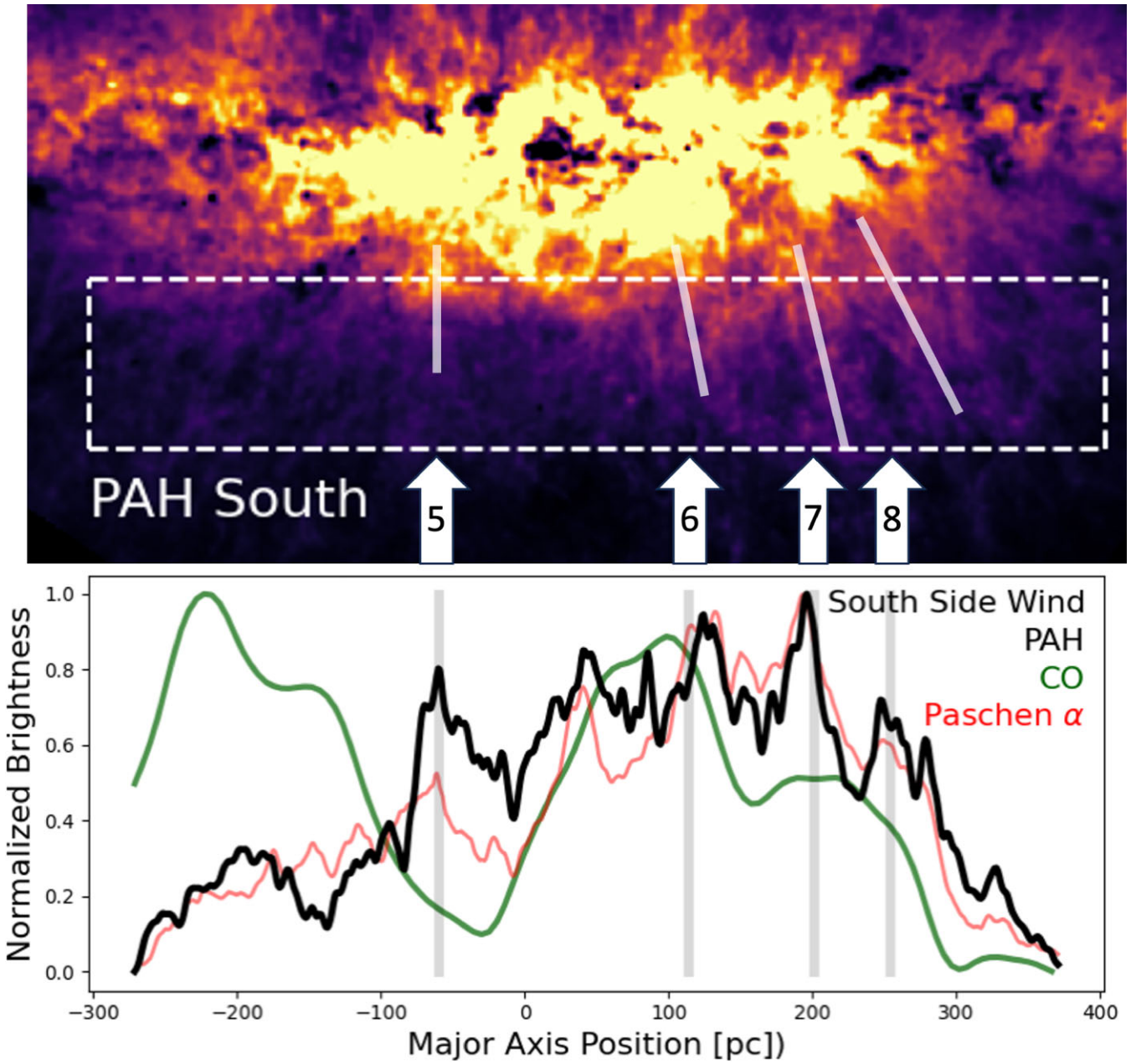

Figure 4. Same as Fig. 3 for southern side of M 82.

in the flux. We find in the normalized brightness profiles that in the region between $z = 80$ pc and 180 pc (shown as boxes in Figs 3 and 4) the typical flux inside the plumes is 2–4 times brighter than in the areas between the plumes.

The location of the peaks in PAH are typically near to peaks in both CO and Pa α. Bolatto et al. (2024) qualitatively discuss the morphological similarity. There is a much tighter relationship 3.3 μm PAH with Pa α than PAH and CO. We expand on PAH–Pa α relationship more in Section 5 of this paper. The 17-times more coarse spatial resolution of the CO data, and the relatively small field of view makes any morphological comparison difficult. In Fig. 3, there are local peaks in CO emission at horizontal positions of −180, −45, and 133 pc. These are all within 10 pc of the centre of PAH plumes.

We now seek to measure the location, size, and shape of the plumes that we identified in Fig. 1. We require a minimum extent for plumes beyond the vertical half-light distance of the starlight in the F250M filter, ∼50 pc. This is intended to select significant plumes, though we acknowledge it is somewhat arbitrarily chosen. The plume does not need to be strictly perpendicular to the disc.

To measure plume properties we select a working window around each candidate. We then search for a significant peak contained within the central 3/4 of the window. This is done for every 0.1 arcsec region moving upward from the disc. If multiple upward steps fail to find a peak, then we identify this as a lack of coherence and the plume measurement is ended. Also, we interpret significant horizontal jumps in the location of the peak (greater than 1/3 the width) as a lack of coherent structure. Once the peak location is identified we define a width. For each row we determine the horizontal distances from the peak that contain 2/3 of the flux in the window. We do not require that the sides of the plume are symmetric. We aim for the local working

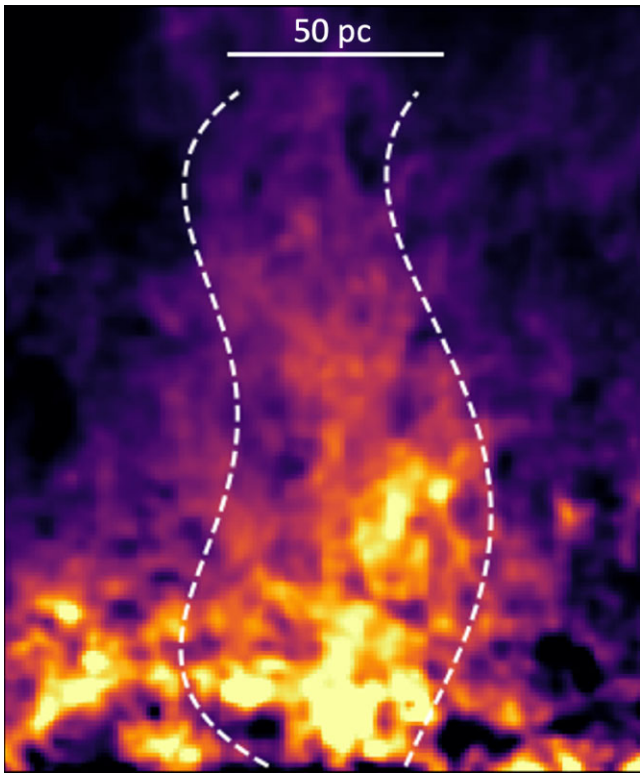

Figure 5. We show Plume-1, as an example of the plume shape and size determination. The local background emission has been subtracted. The white dashed lines represent the polynomial fit to the point-to-point width measurement, which truncates at the bottom of the image. The solid line at the top represents 50 pc.

window, centred on the plume, to be as wide as possible. However, if the working window contains flux from a neighbouring plume, this will impact the width measurement. Future work might investigate simultaneous decomposition of structures. This is, however, beyond the scope of this work. For each plume we iterate the boundary of the working window by ∼3 FWHM of the PSF of the image (20 pixels), and make the final selection on a region that has a stable solution for width and peak locations. After sides are determined for the whole plume we fit a 5th order polynomial to each side of the plume. This is done to smooth the point-to-point scatter in the width measurement. We then calculate the median width of each plume. The uncertainties are simply the root-mean-square deviation across each plume.

There are no regions in our continuum subtracted image that do not have significant PAH emission. The plumes therefore are brighter regions in the total emission field. The choice to subtract a background of lower flux from the plume does impact the measured width. We do not know *a priori* if the plumes are embedded in a background, or rather if it is more correct to treat them as brighter regions in the wind. We therefore provide widths calculated with and without background subtraction. To calculate the background we measure the average flux of the first and last 1 arcsec in each row. On average, plumes are ∼14 pc wider without background subtraction.

In Fig. 5, we show Plume-1 (the left-most plume on the north side of the galaxy) as an example width calculation. In this case, the median width is 60 pc (with background subtracted) and 72 pc with no background removal. This plume extends at least 200 pc, when the image field-of-view ends.

Table 1. The properties of individual plumes identified. We give the position and width for each plume. We provide widths both without and with background subtraction.

Plume	Side	Major axis Position (pc)	Width (pc)	Width Subtracted (pc)
1	North	−190	72 ± 10	60 ± 10
2	North	−43	75 ± 21	56 ± 20
3	North	135	84 ± 25	73 ± 26
4	North	236	67 ± 22	49 ± 32
5	South	−50	79 ± 14	42 ± 10
6	South	92	70 ± 14	57 ± 19
7	South	219	70 ± 9	54 ± 17
8	South	258	45 ± 9	34 ± 10

For completeness, we also investigated peaks in Figs 3 and 4 that did not, ultimately result in a coherent plume. For example, in Fig. 3 there is a peak near to +50 pc. There is no coherent, continuous structure. On the southern side of the galaxy there a number of peaks at major axis offset positions near +90 pc and +270 pc. When placing a window of similar size as others on these regions, however, it does not result in an independent plume.

The average value of the median plume widths is 67 pc wide without background subtraction and 53 pc with background subtraction (see Table 1). We note that this size scale is very well resolved, and not connected to any input parameters of measuring the plume widths. Plumes on the northern side of M 82 are slightly wider than on the southern, with average widths of 59 and 47 pc for north and south (background removed), respectively. As discussed already the major axis offset positions are different, and we find that the southern plumes are less perpendicular to the galaxy major axis. The large scale asymmetry in the M 82 outflow extends down to substructure at the scale of tens of parsec. The plumes on the south side appear to be superimposed on top of a smoother distribution of gas. This is located in a similar region as the CO bubble described in Chisholm & Matsushita (2016). The slightly narrower size of the southern plumes could be due to not being able to separate the lower surface brightness flux from the surrounding fainter emission.

The projection of the plumes and the inclination of M 82 could lead to differences in the measurements of the plumes on the northern and southern sides. M 82 is slightly inclined such that the north side is more visible, whereas parts of the southern side of the disc may be obscured by the galaxy. From imaging alone we cannot know the three-dimensional arrangement of the plumes. However, it seems plausible that some would be further from us than others. This might make it more difficult to observe and measure those on the southern side.

Overall we find that 70 per cent of the flux beyond the central region (±50 pc) is associated with plumes. If the PAHs observed at larger vertical distance from the mid-plane of the galaxy (Engelbracht et al. 2006) are transported from the disc, then these plumes we observe near the galaxy are the dominant lanes of PAH transport and possibly cold gas in general. The rest of the gas, away from the mid-plane, appears in a diffuse form.

We find in our analysis that the flux from several of the plumes extends beyond the field-of-view of our NIRCam observations. In Fig. 6, we replot the PAH emission with the flux scale displayed square-root and the display levels are set to reveal fainter emission. Plumes 1, 2, 4, 5, 7, and 8 extend to the edge of the field-of-view. Plume 2 appears composed of multiple smaller scale filaments, which may be a bubble structure, near the edge of the field. None the less

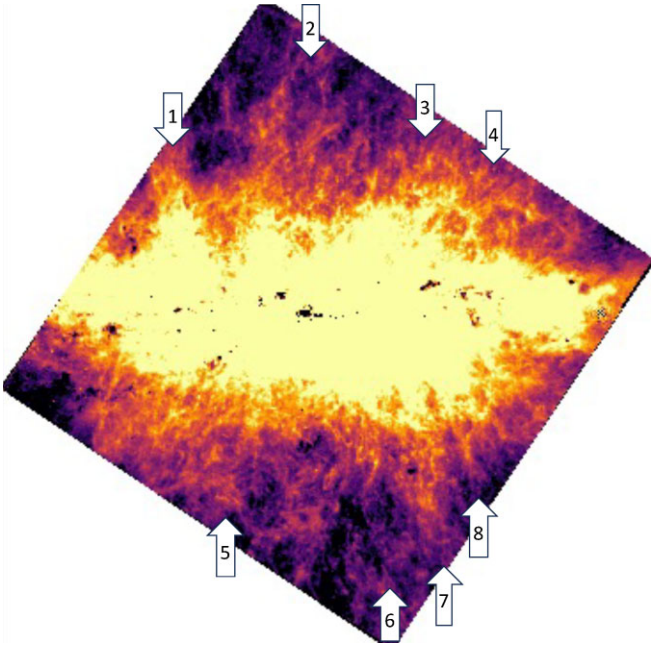

Figure 6. Here, we show 3.3 μm PAH image again, but with the image scale set to square root and the contrast set to show the faintest substructure in the plumes. The locations of the plumes are denoted by arrows. The majority of the plumes extend to the edge of the field of view indicating that their length is greater than ∼300 pc.

a continuous structure can be traced to the edge of the field. This implies that the length of plumes can reach at least to ∼300-400 pc, and likely extend into the larger wind.

The location of PAH plumes and their peaks correlates with the location of peaks in other phases. We see that in Figs 3 and 4. There is a strong correlation of PAH peaks being co-located with Pa α peaks on both the north and south side. In the horizontal flux slice of the plumes (as indicated by grey bars) all are at or near peaks in the normalized Pa α. This similarity in Pa α and 3.3 μm PAH was commented on in Bolatto et al. (2024), and now quantified here. We will investigate the relationship between PAH and Pa α further in a subsequent section. It is difficult to interpret CO in this small image only, as it is 17 times more coarse resolution. Nevertheless in the north outflow there is a connection between peaks in CO and the location of 3 out of 4 chimneys. The large values of CO at the edge of the horizontal surface brightness profiles are well known to be streamers associated with accretion (Walter et al. 2002). In the south side, there is less correspondence with individual peaks, although there is a correlation with the overall rise in CO flux and PAH flux from 0–200 pc in Fig. 4.

4 PARSEC SCALE CLOUDS IN M 82 WINDS

4.1 Identification of clouds

The substructure of the 3.3 μm PAH emission in the M 82 wind is clearly hierarchical. The plumes we describe in the previous section are comprised of a smaller scale substructure. Bolatto et al. (2024) show evidence of this via unsharp masked imaging. We will refer to these smaller features as clouds. The distinction between the clouds and plumes (discussed in the last section) is that multiple clouds may exist within a single plume.

In Fig. 7, we show examples of small-scale clouds of 3.3 μm PAH taken from the plumes in M 82. All of these are located in plumes discussed in the previous section. A common feature of these clouds is a higher surface brightness knot of emission that is followed by a lower surface brightness emission extending away from the galaxy. The clouds are stretched in the vertical axis. A large number of such structures are visible in the M 82 wind, many of which are overlapping in a network, or web-like. At the low surface brightness end of the cloud the distinction between diffuse gas of the plume and the cloud is likely arbitrary. The bright knot typically has 2–4 times the surface brightness of the tail. These outflow clouds can have extents longer than ∼30–150 pc.

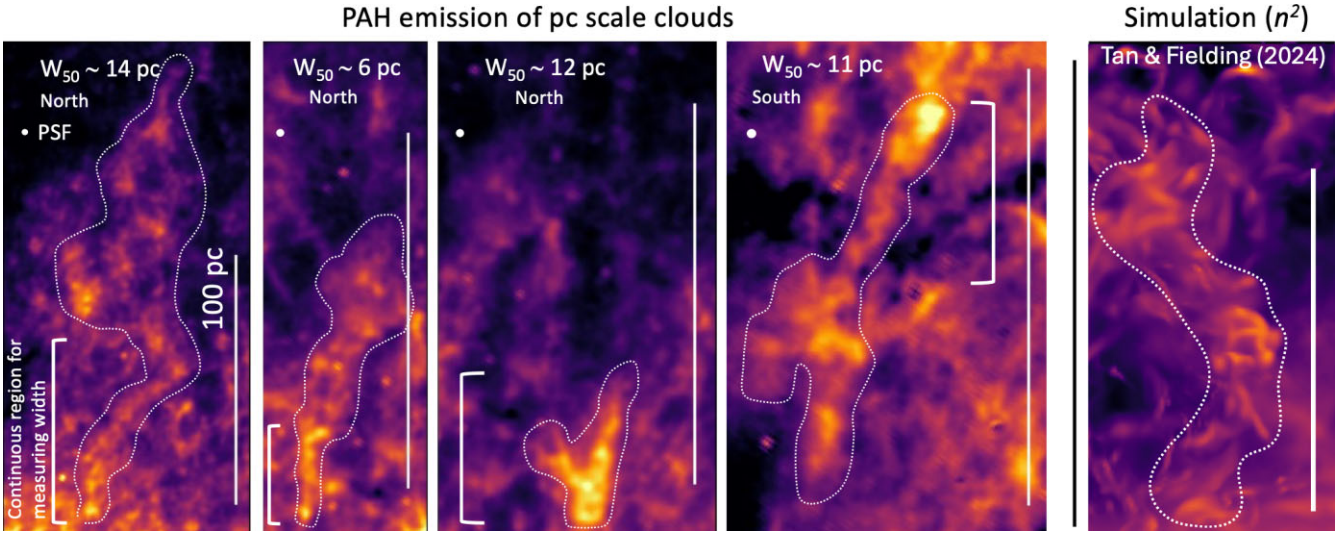

Figure 7. Cutouts of small-scale clouds in M 82 winds. The white bar represents ∼100 pc and the white dot in the upper-left indicates the PSF. The left three panels are taken from the northern side of the outflow, and the second-from-the-right panel from the southern side. The widths containing 50 per cent of the light are listed in the top. For each cloud, we draw a contour that roughly encloses the cloud shape. The vertical bracket on the right side of each panel represents the distance over which the width is estimated. The right-most panel shows a simulation from Tan & Fielding (2024) of a cloud in an outflow. The figure shows density squared. The morphology of the emission is similar to what we observed in M 82.

Our imaging data cannot distinguish if the overlapping structures are truly connected, or if they are unconnected structures superimposed on top of each other. Both scenarios could be true. The latter scenario should be common if the total outflow is arranged in a biconical structure.

A number of simulations in recent years predict that small-scale clouds of cold gas can exist within outflows in a range of environments (Fielding, Quataert & Martizzi 2018; Gronke & Oh 2018; Sparre et al. 2020; Abruzzo et al. 2022; Tan & Fielding 2024; Zhang & Li 2024). Of particular interest to this work is Farber & Gronke (2022), Chen & Oh (2024) and recently Richie et al. (2024). These include rough self-shielding approximations that allow for the formation of colder phases (1000 and 100 K, respectively), which makes them appropriate for comparison to our PAH observations. These simulations adopt a 'cloud-crushing' set up in which an overdense sphere of cold gas is hit by a hot ($\sim 10^6$ K) wind. The general finding is that if cloud size and density are sufficiently large, then the cloud survives the shock and is accelerated by the wind. In the wind, clouds typically stretch into a comet-like structure, with a bright base pointing toward the source of the wind and an extended filamentary tail. The width of the cloud, at least near the base, is similar to the initial cloud diameter. Qualitatively speaking, this structure is what we observe in Fig. 7.

In Fig. 7, we directly compare these small clouds observed in the M 82 outflow to a collection of clouds in the multiphase wind launched in the ISM patch simulation presented in Tan & Fielding (2024). They study cold clouds that emerge from a simulated superbubble in a box with a size of $512\times512\times2048\,\mathrm{pc}^3$. This simulation sits between the idealised 'cloud-crushing' simulations and large-scale full galaxy simulations. They have a comparable spatial resolution to our observations, $\sim$1 pc. The initial conditions of the launching mechanism and disc include clustered supernovae, as would likely happen in the massive star clusters in M 82 (e.g. Levy et al. 2023), coming from a section of a gas disc that has $\Sigma_g \sim 175\,\mathrm{M}_\odot\,\mathrm{pc}^{-2}$. This is a similar, though perhaps slightly lower, surface density to that observed for M 82 (Leroy et al. 2015; Krieger et al. 2021).

Qualitatively speaking, the size and morphology of the 10 pc scale outflow clouds of PAH we observe in M 82 are similar to the clouds simulated in Tan & Fielding (2024). We note that Tan & Fielding (2024) argue that their simulations of clouds validates the qualitative results of the cloud crushing simulations, as well as the more quantitative predictions from detail mixing layer studies (Fielding et al. 2020; Tan, Oh & Gronke 2021).

The spatial resolution of our NIRCam 3.3 μm images allows us to measure sizes larger than $\sim$2 pc in M 82. The white dot in each panel of images in Fig. 7 shows the PSF size. The substructure is marginally resolved. We therefore aim to directly measure the width, which can be related to the physically important $R_{\rm cloud}$. To our knowledge these are the first direct estimates filament widths for clouds embedded in a wind outside of the Milky Way. Other existing estimates of cloud sizes (e.g Xu et al. 2023a) rely on modelling of line ratios.

In order to measure the cloud sizes, we first identify 12 clouds by visual inspection of the full resolution 3.3 μm PAH image. Due to the morphological differences in the northern and southern outflow, we identify six clouds on the northern outflow and six on the southern. We avoid clouds that show significant overlap with other clouds. We also restrict our analysis to clouds that begin at roughly ±200 pc from the mid-plane of M 82.

We caution the reader that these selection criteria almost certainly introduce biases into our sample of clouds. For example, if clouds grow via collisions with other clouds, that may be missed by our selection as they may have more complex structure. Alternatively, there may be a bias in the types of clouds that exhibit cometary structure. The numbers we present should be taken as a first estimate of what is possible. A full analysis of the entire outflow is planned by our team (Arens et al. in preparation).

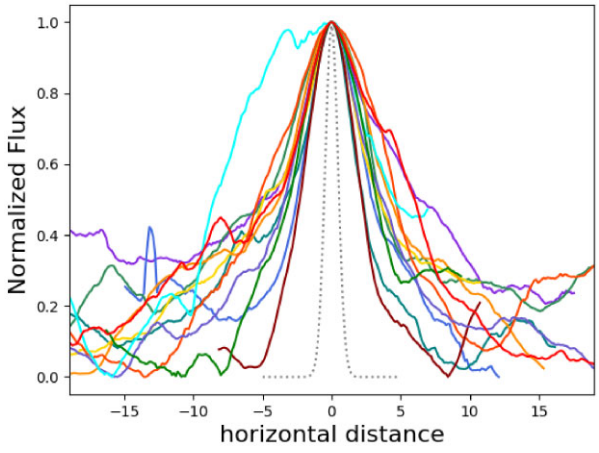

Figure 8. The width of 12 clouds of PAH emission is shown. The colours are arbitrary, so that one can follow individual clouds. The dotted line represents a Gaussian with FWHM$\sim$1.9 pc, which is the nominal spatial resolution. We measure 50 per cent cloud widths of 5–18 pc.

We measure cloud widths in a procedure not unlike that measuring the plume widths. We first define a region bye-eye that includes the cloud (those are shown in Fig. 7) and limits other substructure, and a starting position at the base of the cloud. The software then finds the peak flux in each row. If the position of the peak jumps by more than three PSF FWHM from the previous position the software stops. A normalized surface brightness profile of each row is then determined, with the peak position at $x = 0$ pc. We then take the median of all the resulting rows. Finally, the width of each cloud is taken to be the width that contains 50 per cent of the PAH emission in the normalized median cloud profile. We refer to this width as W_{50}. We show all 12 normalized profiles in Fig. 8. The largest width we measure is $\sim$18 pc and the smallest $\sim$5 pc. There is not a noticeable difference between north and south, though our sample is probably too small to identify any small scale trend. The average width of all twelve clouds is $\sim$9.8 pc.

We can compare these clouds to the cold clouds observed in the fountain of the Milky Way (e.g. Di Teodoro et al. 2020; Noon et al. 2023). Noon et al. (2023) use new, high resolution H I imaging from MeerKAT of three clouds in the Milky Way. They find widths that are similar to ours, $\sim$5–10 pc. Xu et al. (2023b) use optical emission line ratios to derive cloud sizes in M 82. We note that this calculation requires a significant number of assumptions. Moreover, Xu et al. (2023b) make this calculation for optically emitting ionized gas, a different phase of gas that may have different widths from the cold phase studied here. They derive sizes that are $R_{\rm cl}$ $\sim$1 pc. This is smaller than our PAH widths. We do not know, observationally, how the sizes of clouds would change with different phases, although inspection of simulations (e.g. Farber & Gronke 2022; Chen & Oh 2024; Richie et al. 2024) would suggest that the warmer ionized gas would surround the cold gas. Moreover, we state again that our cloud selection may be biased, and may favour larger clouds. Future work, by our team, on the full M 82 outflow imaged at 3.3 μm will allow for a more complete study of cloud widths. Chastenet et al. (2024) studies similar clouds in the galactic fountain of NGC 891. *JWST*

is clearly an excellent tool for studying the small-scale structure of outflow gas. More observations of a range of outflows is now needed to understand the full range of these building blocks of outflows.

4.2 Time-scales for survival of clouds

Theory suggests that the so-called 'cloud crushing time' is a critical parameter to determine the survivability of clouds like those we observe in Fig. 7. This can be estimated as $t_{cc} \sim \chi^{1/2} R_{cloud}/v_{rel}$, where χ is the original density contrast of the cloud to the wind fluid, R_{cloud} is the radius of the cloud, and v_{rel} is the velocity of the cloud relative to the wind fluid. We do not know the original properties of the clouds, but many simulations suggest it is appropriate in wind environments to adopt $\chi \sim 100$–1000 (Gronke & Oh 2018; Sparre et al. 2020; Abruzzo et al. 2022). For M 82 the asymptotic velocity of the hot wind is roughly $v_{hot} \sim 1000\,km\,s^{-1}$ (Strickland & Heckman 2009). We do not know the velocity of the PAH-emitting gas, but we can assume that it moves at a similar velocity to either the ionized gas or the molecular gas. In M 82 ionized gas is known to have $v_{H\alpha} \sim 500\,km\,s^{-1}$ (e.g. Shopbell & Bland-Hawthorn 1998; Xu et al. 2023b). Molecular gas is somewhat slower, observed to have velocities $v_{mol} \sim 200$–$300\,km\,s^{-1}$ (Leroy et al. 2015; Krieger et al. 2021). Given the strong correlation between PAH and Pa α, we take $v_{rel} \sim 500\,km\,s^{-1}$. If the PAH-emitting gas has velocities similar to the gas observed in CO this will increase v_{rel} and thus decrease t_{cc} by roughly a factor of two. Alternatively, if we take the initial velocity of the cloud as the appropriate characteristic this would be significantly lower, $\sim 10\,km\,s^{-1}$, which would imply a higher $v_{rel} \sim 1000\,km\,s^{-1}$ and thus lower t_{cc}. For the size of the cloud, we simply take $R_{cloud,PAH} \sim 2 \times (W_{50}/2) \sim 10$ pc. This yields t_{cc} of order $\sim$0.3–3 Myr.

We can likewise estimate the time needed for the cloud to travel to its current position. The cometary heads of clouds in Figs 7 and 8 are roughly 200 pc from the disc mid-plane. For this, we assume the PAH has roughly similar velocity as the $H\alpha$. This translates to a cloud lifetime of $\sim$0.5–1 Myr. Note if the cloud launches from a higher position than the mid-plane then its lifetime is shorter. The cloud-crushing time is therefore equal to or larger than the lifetime of the cloud, if it originated at the mid-plane. These time-scales are therefore consistent with clouds originating as entrained gas and surviving to this point. We note that our by-eye selection biases our measurement to clouds that, by selection, still exist. An automated analysis of all substructure may find fainter, smaller structures with morphology suggestive of later stages of destruction.

The basic criteria that cooling time of mixed gas is smaller than that of the cloud-crushing time is easily met for M 82. Assuming $n_e \sim 100\,cm^{-3}$ (e.g. Xu et al. 2023b) for 10^4 K gas the typical pressure is $P/k_b \sim 10^6$ cm^{-3} K, which corresponds to $t_{cool,mix} \sim 10^{-4}$ Myr (Abruzzo et al. 2022). Thus these cloud sizes are more than sufficient to survive the disc breakout. Likewise, Bolatto et al. (2024) discuss the time-scale for PAHs to be destroyed in M 82 wind. Calculations for collisional destruction of PAHs suggest that those time-scales are long, in excess of 10 Myr (Micelotta, Jones & Tielens 2010). Photodestruction time-scales are very uncertain, particularly for PAHs embedded in ionized gas, but they may be considerably shorter. PAHs in the ionized gas, however, may be constantly replenished as neutral gas is ionized, for as long as a neutral or molecular gas reservoir exists.

Cloud sizes are very important to establish t_{cc}, and we could have underestimated those in our calculations above. A plausible scenario is that the cold gas we trace with PAH is surrounded by warmer ionized gas. The majority of simulations and theory surrounding cloud crushing focuses on gas that is above 10^4 K, which would be more likely ionized. Those simulations that do consider low temperature gas (Farber & Gronke 2022; Chen & Oh 2024) show temperature gradients such that the coldest gas is concentrated in the middle of the cloud. This would imply a larger R_{cloud} and thus a larger t_{cc}. Also, the simulations of both Chen & Oh (2024) and Farber & Gronke (2022) consider pressures that are multiple orders of magnitude smaller than what is observed in M 82. This generates clouds that are larger, following Abruzzo et al. (2022). In principle, we expect that if simulations of cold gas are run that match the conditions of M 82 they may indeed generate cloud sizes more similar to ours. Alternatively, if we have underestimated v_{rel}, either from underestimating the velocity of the hot wind or overestimating the velocity of the cold gas, then this would reduce t_{cc}, and suggest that these clouds should be more rare at larger distance.

Overall, we take these results as encouraging for the picture of cloud entrainment and survival. First, the morphological similarity of our clouds to those produced in cloud-crushing simulations suggests that the overall concept may be valid. Moreover, we have demonstrated that the cloud properties observed in the M 82 wind are consistent with what theory predicts is required for a cloud to survive breakout from the disc without being shredded by the hot wind.

5 CORRELATION OF PAH AND PA α IN BOTH MID-PLANE AND OUTFLOW

In Section 3, we discuss the connection between the location of the plumes in PAH and the colocation of peaks in the Pa α image. In Fig. 9 we investigate this further showing the pixel-to-pixel correlation of 3.3 μm PAH emission with that of Pa α. The 3.3 μm PAH feature is generally understood to arise from small, neutral PAHs (Draine et al. 2021), and thus does not *a priori* require strong correlations with ionised gas. Indeed, recent observations of the Orion Bar, with much finer (milliparsec) resolution, show that 3.3 μm emission decays where Pa α is brightest (Peeters et al. 2024).

For our analysis the PAH image is convolved and resampled to match the NIC3 F187N observations. The FWHM of NIC3 is $\sim$0.35 arcsec ($\sim$6 pc). This is sufficient to identify the plumes. At the small scale cloud substructure, roughly half the cloud would be covered by a single resolution element. It is, therefore, more difficult with this spatial resolution to separate a cloud from the background emission.

We note that in Figs 3 and 4 the brightest parts of the PAH emission, which are in the centre of the disc, are blacked out. This is due to oversubtraction of the continuum on the 3.3 μm PAH. The continuum subtraction procedure from Bolatto et al. (2024) is optimized for the wind emission. It is unlikely that the same scale-factors are applicable in the disc as in the wind. This is due both to the variations in stellar populations, but also in the water absorption.

We did not apply an extinction correction to Paschen α, as it is difficult to make pixel-to-pixel estimates in the mid-plane of the highly extincted M 82, with studies finding variation in the disc of $A_V \sim 2$–12 mag (e.g. Förster Schreiber et al. 2001). The extinction will be significantly higher at 1.87 μm than at 3.3 μm, and has been observed to decrease as a function of distance from the galaxy (Westmoquette et al. 2013). It is reasonable to expect from a foreground screen model that in the centre of M 82 the extinction correction will result in Pa α fluxes that are a factor of $\sim$5–10 brighter, but PAH fluxes only increase by factors of $\sim$1.5–2 (Förster Schreiber et al. 2001; Draine 2003). In the outflow, there will be negligible extinction (Westmoquette et al. 2013). The trends

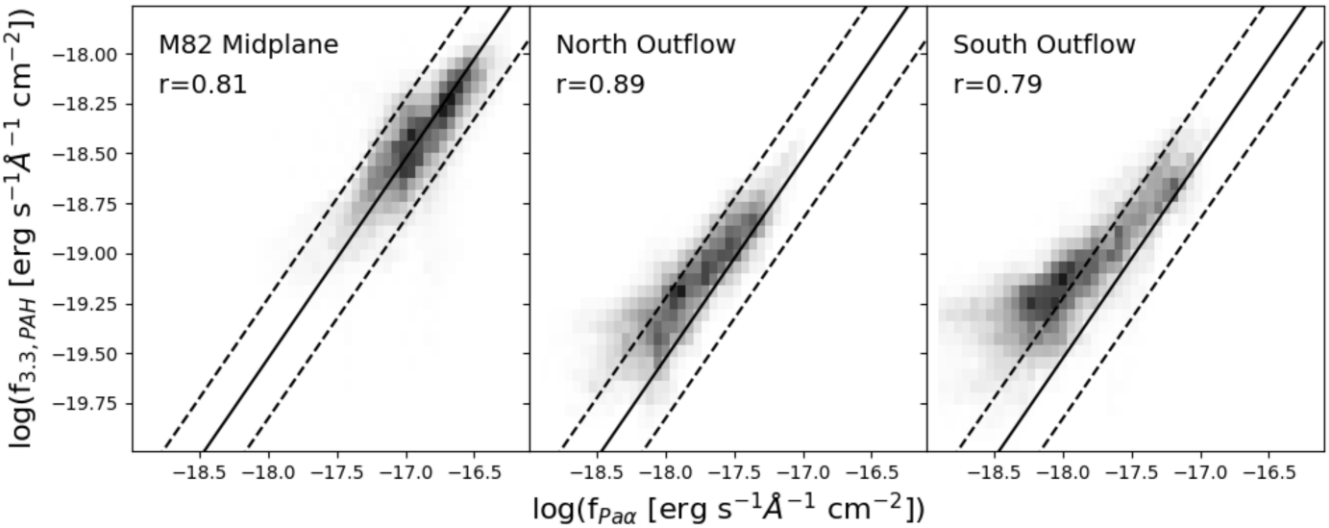

Figure 9. The relationship between PAH flux and Paschen α is shown for the centre of M 82 (left), the northern outflow (middle), and the southern outflow (right). The greyscale is a histogram of the number of points in each bin. In each plot, we show the relationship derived for the centre of M 82 as a black solid line. The grey scale histograms indicates the number of points in each bin. In all panels there is a strong correlation between the gas tracers. There is an elevation of PAH flux compared to Paschen α in the outflow regions.

of increasing PAH/Pa α with distance from the mid-plane, which we describe below, could be steeper due to extinction.

In Fig. 9, we show that there is a very strong correlation between PAH and Pa α emission in both the mid-plane and outflow of M 82. We find Pearson's correlation coefficients of $r = 0.8$–0.9 for each component of this galaxy. The grey scale in the figure represents a histogram of the frequency of each value, and is generated from a 50×50 grid in log space covering $\log(f_{\mathrm{Pa}\,\alpha}) = -19$ to -16 and $\log(f_{3.3,\mathrm{PAH}}) = -20$ to -17. In the galaxy mid-plane there is $\sim$0.2 dex scatter around a linear relationship. Similarly, Belfiore et al. (2023) studies 3.3 µm emission toward H II regions in PHANGS galaxies, with spatial resolution of order $\sim$15–50 pc (see also review by Schinnerer & Leroy 2024). The correlation in our figure suggests that 3.3 µm feature does not experience as strong a PAH decrement in bright H α-emitting H II regions as other PAH features show (e.g. Gordon et al. 2008; Egorov et al. 2023). However, we remind the reader that the extinction effects could impact this by increasing the Paschen α relative to the PAH by a factor of several. We cannot say how this translates to the results of Egorov et al. (2023). Our strong correlation in the mid-plane of M 82 is, none the less, not unlike the behaviour of H II regions in the PHANGS survey.

In the middle and right panels of Fig. 9, we find that the relationship between 3.3 µm PAH and Pa α remains strong ($r \sim 0.8$–0.9) in the outflow. There is, however, an increase in $f_{3.3}/f_{\mathrm{Pa}\alpha}$ in both the northern and southern outflows relative to the relation observed in the mid-plane. This ratio also increases for lower PAH and Pa α fluxes. We find that in the mid-plane of M 82 $\log(f_{3.3}/f_{\mathrm{Pa}\alpha}) \sim -1.6$. This increases in the wind to ~-1.3 (north side) and ~-1.15 (southside). The relationship between 3.3 µm PAH and Pa α in the north outflow remains closer to linear, while in the south there is shallower a slope of $f_{3.3}$ with $f_{\mathrm{Pa}\alpha}$.

There is a dependence in both the observed PAH and Pa α fluxes with distance from the mid-plane, and therefore decreasing flux is essentially equivalent to increasing distance from the mid-plane within our field of view. We show this in Fig. 10. Here, we plot the $f_{3.3}/f_{\mathrm{Pa}\alpha}$ for each plume identified in Section 3 of this paper. In all plumes the $f_{3.3}/f_{\mathrm{Pa}\alpha}$ ratio increases from the mid-plane to a position of

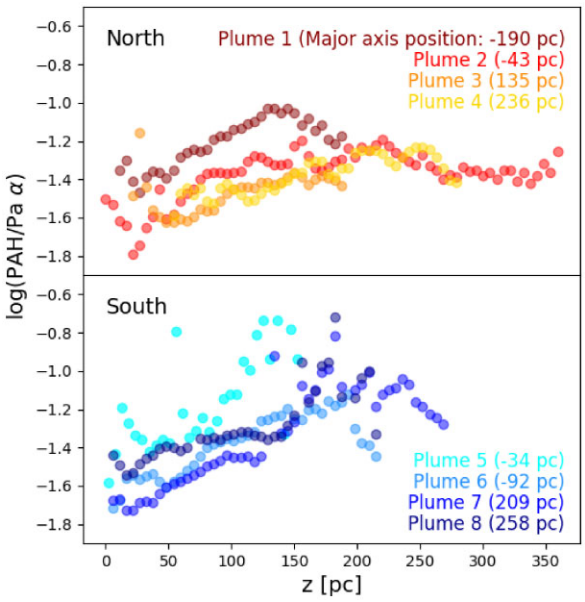

Figure 10. The PAH/Pa α flux ratio for each of the plumes identified in Section 3 is plotted the distance to the mid-plane of the galaxy. North and south outflows are plotted in top and bottom panels, respectively. We see an increasing ratio with distance from the galaxy.

$|z| \sim 100$–150 pc from the disc. Only a few plumes are measurable beyond this. Plumes 1, 2, 4, and 7 seem to no longer show an increase in $f_{3.3}/f_{\mathrm{Pa}\alpha}$ beyond this position. We remind the reader that any effort to correct for extinction will make this difference between the mid-plane and outflow more extreme, as the ratio of PAH-to-Pa α will decrease in the galaxy centre. Applying the assumptions described above the value of PAH-to-Pa α at $z = 0$ could be a factor of four lower than what is shown in the figure, especially for those plumes at major axis positions closer to the galaxy centre (2 and 5).

Overall, we can place the observed relationship of 3.3 µm PAH and Pa α in the context of recent observations of spiral galaxies.

In local spirals from the PHANGS survey observations show tight relationships between extinction corrected H α and PAH emission lines (Belfiore et al. 2023; Leroy et al. 2023; Schinnerer & Leroy 2024). This is very similar to our relationship in Fig. 9.

We find that in the central starburst of M 82, $L_{\rm PAH}$(F335M) $\approx 17 L$(Pa α). It is difficult to interpret any comparison of this to similar results of correlations of PAH features with Balmer lines (e.g. Belfiore et al. 2023; Leroy et al. 2023; Schinnerer & Leroy 2024). The central starburst of M 82 is very different than H II regions, which the PHANGS measurements are based on. Our ratio of $L_{\rm PAH}$(F335M)/L(Pa α) is lower by a factor of ~5-6 compared to the PHANGS. We remind the reader that correcting for extinction makes this discrepancy between M 82 and PHANGS galaxies more extreme. The low value of our number may indicate a larger amount of diffuse ionized gas along the line of sight. The orientation of M 82 likewise complicates this comparison, as PHANGS galaxies are face-on and M 82 is edge-on. Further investigation of starburst galaxies will be informative. Independent of any decrement in PAH emission, what Fig. 9 clearly demonstrates is a strong correlation of PAH and ionized gas flux in a broad range of galaxy types.

Based on observations of PHANGS galaxies, Leroy et al. (2023) argue that the emission of mid-IR features, like 3.3 μm PAH, is driven by a mixture of heating (traced by ionized gas) and column density of cold gas. Our results in Figs 9 and 10 can be understood in this framework. The tight correlation of Pa α and PAH in the mid-plane of M 82 suggests that heating is dominating the emission. As we move to larger distances from the galaxy the heating sources decrease. This is observed as a decrease in the median Pa α surface brightness by roughly an order of magnitude in the outflow compared to the mid-plane. This is similar to PHANGS observations (Leroy et al. 2023), where gas with fainter H α emission has higher ratios of PAH/H α, in that case using the 7.7 μm and 11 μm emission. As the ionized gas flux decreases the relative importance of cold gas column density increases. Future work using the larger field-of-view observations of M 82 and more PAH emission lines will be informative to compare to this model.

6 PAH EMISSION IS FAINTER IN BRIGHT X-RAY REGIONS OF THE M 82 WIND

In Fig. 11, we compare the horizontal flux profiles of 3.3 μm PAH and CO(1–0) to the X-ray emission (taken from Lopez et al. 2020). A commonly adopted picture of the multiphase structure of outflows is one in which the hot X-ray gas establishes a central lobe that is surrounded by colder gas (e.g. Leroy et al. 2015). Our *JWST* NIRCam observations allow us to resolve the relation between PAH-emitting cool gas and X-ray emitting hot gas on small scales.

The bottom panels of Fig. 11 shows that in the mid-plane of M 82 X-ray and PAH emission overlap. There is a strong X-ray peak at major-axis position −50 pc, which corresponds to a local peak in PAH emission. This behaviour changes in the outflow, although the pattern is somewhat different on the north and south sides of the galaxy. We will, therefore, describe these separately.

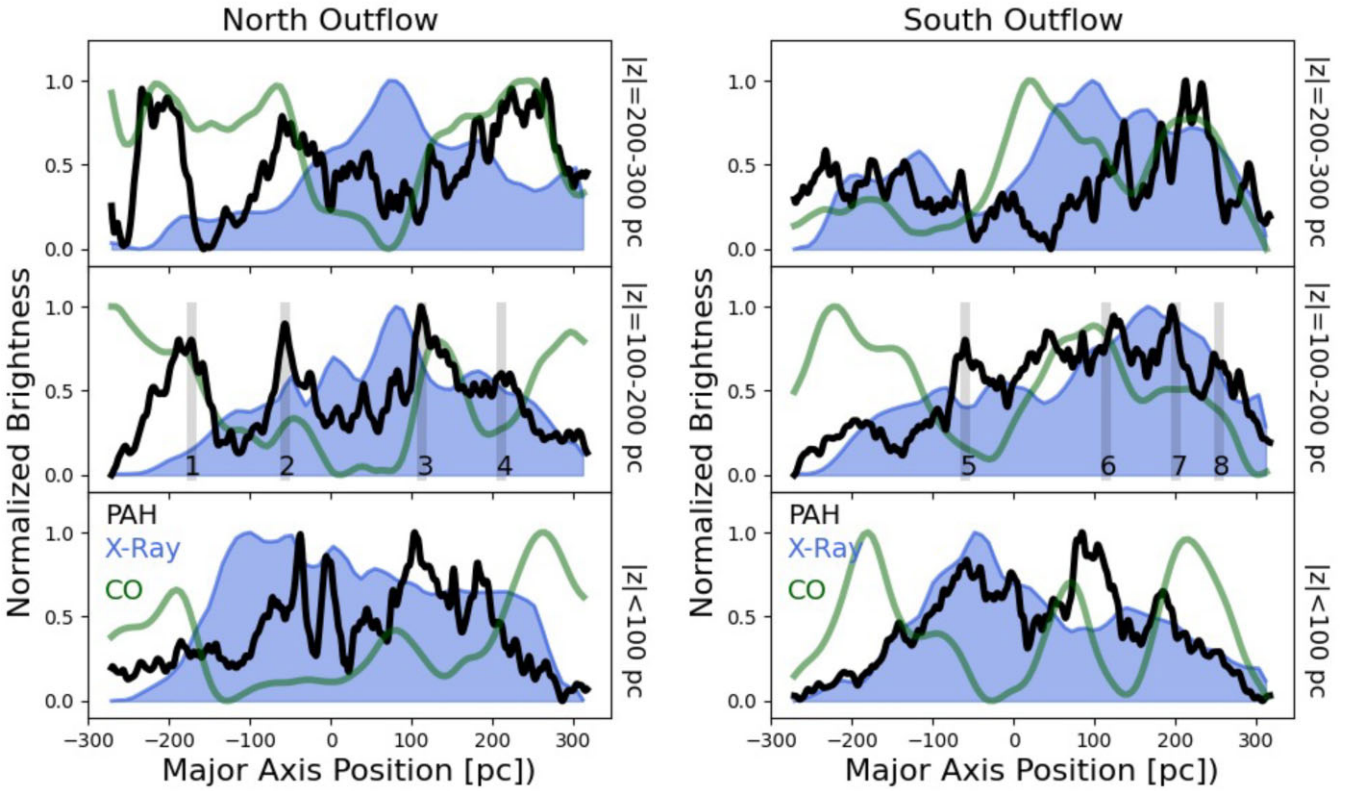

Figure 11. Similar to Fig. 3, we show the normalized horizontal profile of the PAH flux (black) and the CO(1–0) flux (green). In this figure, we add the X-ray flux (blue) from Lopez et al. (2020). The middle panel is a similar region as in Figs 3 and 4 on the left and right, respectively. The bars in the middle panel show the location of the PAH plumes. We also show the galaxy centre and a region at higher elevation than the middle panel. These profiles establish that the well-known picture in which cold gas surrounds a hot wind establishes itself within a few hundred parsec and is important for setting the morphology of the PAH plumes.

6.1 North outflow

On the north side of M 82 (Fig. 11 left) the difference in spatial distribution between X-ray and PAH emission becomes apparent within 100 pc of the galaxy mid-plane. The brightest X-ray peak in this z-axis elevation is located at a major axis offset of +80 pc from the galaxy centre with emission falling off at larger offsets. Two PAH plumes surround this central peak, located at roughly −55 pc and +110 pc offsets. There is a local trough in the PAH emission between these two plumes, the location of which corresponds to the X-ray peak. As we have shown in Fig. 3 the peaks in CO(1–0) are spatially correlated with PAH. Now we show that peaks of both CO(1–0) and PAH are separated from the X-ray peak. The rest of the PAH emission plumes are found at larger major axis offsets from the X-ray peak.

At the farthest distance from the starburst ($z \sim$ 200–300 pc), both the PAH and CO emission shows a local minimum value at the location of the X-ray peak. The peak in X-ray is colocated with the lowest brightness of CO in this region. Plume-3 at $z \sim$ 100–200 (located closest to the X-ray peak, at offset +110 pc) is no longer prominent, although there is still a local peak at the offset position of Plume-3. Prominent PAH emission plumes on the north side of the outflow are at offsets of ∼150–200 pc from the X-ray peak. At this distance above the plane, the CO has its minimum at the same location as the X-ray peak.

6.2 South outflow

The difference in position of peaks between X-ray and PAH emission does not develop as near to the galaxy mid-plane in the south outflow as in the north. In the $z \sim$ 100–200 pc range on the south the peak in X-ray emission is located at a major axis offset of +167 pc from the galaxy centre. This peak is broader than the peak on the northern side. The X-ray, CO, and PAH emission peaks on the south side all overlap. We noted above that the southern plumes are less perpendicular to the galaxy major axis, closer together and less prominent than those on the north. The coincidence with the hot wind may be related to this.

At larger distances from the galaxy mid-plane ($|z| \sim$ 200–300 pc) the southern outflow behaves more similar to the north. The X-ray peak moves to ∼100 pc and is narrower. The PAH emission no longer peaks at the same location as the X-ray. The most prominent PAH peak is at an offset of ∼+210 pc, at least 100 pc away from the X-ray peak. Conversely, Plume-6, located nearest to the X-ray peak at $z \sim$ 100 pc, is no longer as prominent as Plumes 7 and 8 at $z >$ 200 pc. Because the southern PAH plumes diverge away from the galaxy centre, Plumes 7 & 8 are therefore, also diverging away from the X-ray peak at this height. There is another CO peak at 20 pc, that likewise is not colocated with the X-ray peak, though is not colocated with a local PAH peak either.

In both the north and the south outflows by $z \sim$ 200–300 pc there seems to be an established separation along the observed major-axis between the brightest regions of the X-ray and the brightest PAH emission. This is a change in behaviour from the mid-plane gas ($|z| <$ 100 pc). On the north side this happens as low as ∼100 pc from the mid-plane. Previous work (e.g. Engelbracht et al. 2006; Strickland & Heckman 2009; Leroy et al. 2015) has shown that the projected separation of hot X-ray gas from colder phase gas exists at large distances from the galaxy. Our *JWST* observations show that this separation establishes within 100 pc after breakout from the disc.

To interpret the locations of the peaks in terms of a physical picture requires us to assume a three-dimensional geometry and projection of that geometry on the two-dimensional image. We note that because M 82 is highly inclined we do not know the relative position of the PAH plumes and X-ray emission along the line-of-sight. The simplest case is one in which all hot gas and cold gas is ejected from the galaxy together and there is little interaction between the hot and cold gas. In this case, one would expect the brightness of the colder phases to be similar in the disc and in the outflow and for them to be centrally peaked and decay at larger major-axis position, like the X-rays. The different positions of peaks of X-ray and PAH emission for both north and south sides of the wind at $z >$ 200 pc makes this scenario inconsistent with our data.

We also consider the popular picture in which the outflow of M 82 consists of a hot inner component and cooler gas on the outer parts. In this picture, the plumes at the edges of the field could be interpreted as limb-brightening. However, the plumes closer to the centre of the major-axis are not likely to be limb-brightened. A scenario consistent with this on the north side of M 82 is that Plumes 2 and 3 (the two plumes closest to the galaxy centre) are located further from the galaxy centre along the line-of-sight than their major axis position. In this case, the cold gas would surround the hot wind. If this is true, then the observed position of the inner plumes then depends on our viewing angle. Observations of more galaxies with outflows are therefore needed, as we would expect a range of plume distances along the major-axis of the galaxy.

In summary, our key observation of the relationship between the PAH emission and that of the hot X-ray gas is (1) that the correlation changes from the mid-plane of the disc and the outflow. In the disc, the horizontal profile of PAH and X-rays are similar. This changes in the outflow, which leads to the second key result, (2) that for gas above $|z| >$ 200 pc, the brightness of X-ray gas peaks correspond to local minima of the PAH brightness. We note this is different to the relationship between PAH and Pa α and suggests a phase structure to the outflow.

7 SUMMARY AND CONCLUSIONS

The 3.3 μm PAH emission ejected from the starburst of M 82 is not a smooth structure, it is organized in plumes and those plumes are composed of smaller scale clouds (some with identifiable cometary shapes). We find that the plumes have widths of order ∼50–75 pc. We identify four coherent plumes on each side of the galaxy. At least one plume on the north side merges with adjacent emission and there are other structures on the south side with similar widths that are shorter. The identified plumes comprise 70 per cent of the 3.3 μm flux. We find that most of the plumes extend to the edge of our field of view. We suggest that plumes may be the dominant method by which cool gas is transported to large distances from the starburst by the wind.

These plumes, therefore, should be reproduced by simulations of winds that are intended to describe outflows like M 82. For example, recent simulations show that the impact of cosmic rays is to smooth out the clumpy substructure (e.g. Rathjen et al. 2021). Our observations may indicate that, while cosmic rays may play an important role in Milky Way-like environments (Armillotta, Ostriker & Jiang 2022), they are less important when the starburst is as strong as in M 82. This can be tested with *JWST* observations of nearby edge-on systems with low star formation rates.

We find that the locations of the PAH plumes are likewise the locations of brighter Pa α (Figs 3 and 4). Moreover, we show that in pixel-to-pixel comparison there is a tight correlation of 3.3 μm PAH flux with Pa α flux (Fig. 9). Our interpretation of this is that the plumes in PAH emission are also likely substructures in ionized

gas, likely arising at the photoionized surfaces of neutral or molecular clouds. Comparison to CO emission is hampered by the lower spatial resolution and sensitivity of the available data, although there do seem to be local peaks in CO that are co-located with the PAH emission plumes. Bolatto et al. (2024) show that these plumes also are co-located with bright plumes in 6 GHz radio continuum, caused by free–free emission.

We show in Fig. 7 that the plumes are comprised of smaller clouds that often have an elongated structure with a bright base in the direction of the starburst. We note the similarities between this cometary shape and those results of cloud-crushing simulations (e.g. Armillotta et al. 2017; Gronke & Oh 2018; Sparre et al. 2020; Abruzzo et al. 2022; Farber & Gronke 2022). We measure the widths of 12 clouds selected from the image, finding a typical width ∼5–18 pc, with an average of 9.8 pc (Fig. 8). Taking this to indicate the cloud size we estimate the cloud crushing time-scale $t_{cc} \sim 15$ Myr. This changes by a factor of ∼2 depending up assumptions of initial cloud overdensity and wind speed. Our selected clouds are all taken from distances $z \sim 200$ pc from the mid-plane. We find that t_{cc} is very similar to the traveltime of the cloud from the galaxy mid-plane, assuming a velocity of order 500 km s^{-1}. The general prediction of simulations is that, absent stabilization mechanisms such as cooling, cold clouds are destroyed on a time-scale of a few t_{cc}. We selected clouds that were fairly isolated and with sufficient signal-to-noise to measure the size, which possibly biases us to more prominent, possibly more intact, clouds. Nevertheless, these sizes are consistent with a picture in which the cool clouds entrained in the outflow survive for some time in the wind.

A straightforward interpretation of the plumes extending outward from the disc and the viability of cloud survival time-scales is that the clouds we observe at 200–300 pc in M 82 are entrained in the hot flow within the disc and transported outward. We take these results as strongly encouraging further work on cold gas clouds in galaxy winds. Only a few works (Farber & Gronke 2022; Chen & Oh 2024; Richie et al. 2024) reach sufficiently low temperatures (∼10^2–10^3 K) to include dust physics, while the ability of *JWST* to identify these structures motivates a need for more simulations of dust and molecular gas in outflows.

Increasing the temperature of the wind means that the minimum cloud size that survives will likewise increase (Gronke & Oh 2018). If those clouds are located in plumes of cold gas it is plausible that the surrounding gas is cooler. The results of Fig. 11 suggest that indeed the PAH resides in locations of cold gas. The strong correlations of PAH and Paschen α at scales of ∼5 pc can be understood if the PAH emission is coming mostly from gas at the photodissociation region, close to the photoionized gas (which itself is only 3000–10000 K, still much cooler than the X-ray emitting gas). The colocation of the PAH peaks and the CO peaks suggest that in the plume environment the local gas temperature is lower, thus allowing cold clouds to more easily survive. Several works are in progress to study the PAH emission in the full field of view of M 82 (Villanueva et al. in preparation, Lopez et al. in preparation, Arens et al. in preparation, Cronin et al. in preparation). The hierarchical structure of small scale clouds, residing in plume super-structures, may be necessary to transport cold gas from the disc to the outflow. The 3.3 μm PAH feature is the best high-spatial resolution tracer of cold gas in the diffuse environment of outflows. *JWST* observations of 3.3 μm PAH in more galaxies with galactic winds are clearly needed.

The observations we present here are a starting point, while many questions still remain. How common is the substructure we identify in M 82? Are the plumes and clouds common features of galactic winds? Is this substructure only a feature of starbursts, or does it extend to lower speed galactic fountains in main-sequence discs, where cosmic rays may be more important? Large scale galaxy evolution simulations find that galactic winds are the dominant mechanism to regulate galaxy growth (Naab & Ostriker 2017; Pillepich et al. 2018). Observations, however, suggest that very little of the outflow gas fully escapes the halo (Chisholm et al. 2015; Heckman et al. 2015; Davies et al. 2019; Marasco et al. 2023). The energetics of the outflow are crucial to regulating star formation, and current theory suggest the small-scale structure of the cold gas is vital to setting those energetics (Fielding & Bryan 2022). *JWST* opens a window to the small-scale building blocks of galactic outflows – more observations of PAH emission in such objects will allow us to build better models of galaxy evolution.

ACKNOWLEDGEMENTS

The authors are grateful to Max Gronke whose conversations aided the writing of this paper. This work is based on observations made with the NASA/ESA/CSA *JWST*. The data were obtained from the Mikulski Archive for Space Telescopes at the Space Telescope Science Institute, which is operated by the Association of Universities for Research in Astronomy, Inc., under NASA contract NAS 5–03127 for *JWST*. These observations are associated with programme *JWST*-GO-01701. Support for programme JWST-GO-01701 is provided by NASA through a grant from the Space Telescope Science Institute, which is operated by the Association of Universities for Research in Astronomy, Inc., under NASA contract NAS 5–03127.

DBF acknowledges support by the Australian Research Council Centre of Excellence for All Sky Astrophysics in 3 Dimensions (ASTRO 3D), through project number CE170100013 and from Australian Research Council Future Fellowship FT170100376.

ADB and SAC acknowledge support from the NSF under award AST-2108140.

RCL acknowledges partial support for this work provided by a NSF Astronomy and Astrophysics Postdoctoral Fellowship under award AST-2102625.

LAL and SL acknowledge support from the Heising-Simons Foundation grant 2022–3533 and NASA's Astrophysics Data Analysis Programme under grant number 80NSSC22K0496. This work was also supported by NASA through *Chandra* Award Number AR4-25007X issued by the *Chandra* X-ray Center, which is operated by the Smithsonian Astrophysical Observatory for and on behalf of the National Aeronautics Space Administration under contract NAS8-03060.

IDL acknowledges funding support from the European Research Council (ERC) under the European Union's Horizon 2020 research and innovation programme DustOrigin (ERC-2019-StG-851622) and funding support from the Belgian Science Policy Office (BELSPO) through the PRODEX project '*JWST*/MIRI Science exploitation' (C4000142239).

RSK and SCOG acknowledge funding from the European Research Council via the Synergy Grant 'ECOGAL' (project ID 855130), from the German Excellence Strategy via the Heidelberg Cluster of Excellence (EXC 2181–390900948) 'STRUCTURES', and from the German Ministry for Economic Affairs and Climate Action in project 'MAINN' (funding ID 50OO2206).

VV acknowledges support from the scholarship ANID-FULBRIGHT BIO 2016–56160020, funding from NRAO Student Observing Support (SOS) – SOSPADA-015, and funding from the ALMA-ANID Postdoctoral Fellowship under the award ASTRO21-0062.

LL acknowledges that a portion of their research was carried out at the Jet Propulsion Laboratory, California Institute of Technology, under a contract with the National Aeronautics and Space Administration (80NM0018D0004).

RH-C thanks the Max Planck Society for support under the Partner Group project 'The Baryon Cycle in Galaxies' between the Max Planck for Extraterrestrial Physics and the Universidad de Concepción. RH-C also gratefully acknowledge financial support from ANID–MILENIO – NCN2024_112 and ANID BASAL FB210003.

DATA AVAILABILITY

JWST data used in this will be available in the *JWST* MAST archive. The *HST* images are available in *HST* MAST archive. All other data is published.

REFERENCES

Abruzzo M. W., Bryan G. L., Fielding D. B., 2022, ApJ, 925, 199
Alonso-Herrero A., Rieke G. H., Rieke M. J., Kelly D. M., 2003, AJ, 125, 1210
Armillotta L., Fraternali F., Werk J. K., Prochaska J. X., Marinacci F., 2017, MNRAS, 470, 114
Armillotta L., Ostriker E. C., Jiang Y.-F., 2022, ApJ, 929, 170
Belfiore F. et al., 2023, A&A, 678, A129
Böker T. et al., 1999, ApJS, 124, 95
Bolatto A. D., Wolfire M., Leroy A. K., 2013a, ARA&A, 51, 207
Bolatto A. D. et al., 2013b, Nature, 499, 450
Bolatto A. D. et al., 2024, ApJ, 967, 63
-Bushouse H. et al., 2023, JWST Calibration Pipeline. Zenodo. Available at:https://doi.org/10.5281/zenodo.6984365
Chastenet J. et al., 2024, A&A, 690, A348
Chen Z., Oh S. P., 2024, MNRAS, 530, 4032
Chevalier R. A., Clegg A. W., 1985, Nature, 317, 44
Chisholm J., Matsushita S., 2016, ApJ, 830, 72
Chisholm J., Tremonti C. A., Leitherer C., Chen Y., Wofford A., Lundgren B., 2015, ApJ, 811, 149
Davies R. L. et al., 2019, ApJ, 873, 122
Di Teodoro E. M., McClure-Griffiths N. M., Lockman F. J., Armillotta L., 2020, Nature, 584, 364
Draine B. T., 2003, ARA&A, 41, 241
Draine B. T., Li A., Hensley B. S., Hunt L. K., Sandstrom K., Smith J. D. T., 2021, ApJ, 917, 3
Egorov O. V. et al., 2023, ApJ, 944, L16
Engelbracht C. W. et al., 2006, ApJ, 642, L127
Farber R. J., Gronke M., 2022, MNRAS, 510, 551
Fielding D. B., Bryan G. L., 2022, ApJ, 924, 82
Fielding D., Quataert E., Martizzi D., 2018, MNRAS, 481, 3325
Fielding D. B., Ostriker E. C., Bryan G. L., Jermyn A. S., 2020, ApJ, 894, L24
Förster Schreiber N. M., Genzel R., Lutz D., Kunze D., Sternberg A., 2001, ApJ, 552, 544
Fraternali F., 2017, in Fox A., Davé R., eds, ASP Conf. Ser. Vol. 430, Gas Accretion onto Galaxies. Astron. Soc. Pac., San Francisco, p. 323
Freedman W. L. et al., 1994, ApJ, 427, 628
Gordon K. D., Engelbracht C. W., Rieke G. H., Misselt K. A., Smith J. D. T., Kennicutt R. C., Jr, 2008, ApJ, 682, 336
Gronke M., Oh S. P., 2018, MNRAS, 480, L111
Gronke M., Oh S. P., 2020, MNRAS, 492, 1970
Heckman T. M., Armus L., Miley G. K., 1990, ApJS, 74, 833
Heckman T. M., Alexandroff R. M., Borthakur S., Overzier R., Leitherer C., 2015, ApJ, 809, 147
Hopkins P. F., Quataert E., Murray N., 2012, MNRAS, 421, 3488
Klein R. I., McKee C. F., Colella P., 1994, ApJ, 420, 213
Krieger N. et al., 2021, ApJ, 915, L3
Lai T. S. Y., Smith J. D. T., Baba S., Spoon H. W. W., Imanishi M., 2020, ApJ, 905, 55
Leroy A. K. et al., 2015, ApJ, 814, 83
Leroy A. K. et al., 2023, ApJ, 944, L9
Levy R. C. et al., 2023, ApJ, 958, 109
Lopez L. A., Mathur S., Nguyen D. D., Thompson T. A., Olivier G. M., 2020, ApJ, 904, 152
Lynds C. R., Sandage A. R., 1963, ApJ, 137, 1005
Marasco A. et al., 2023, A&A, 670, A92
Martini P., Leroy A. K., Mangum J. G., Bolatto A., Keating K. M., Sandstrom K., Walter F., 2018, ApJ, 856, 61
McCormick A., Veilleux S., Rupke D. S. N., 2013, ApJ, 774, 126
McQuinn K. B. W., van Zee L., Skillman E. D., 2019, ApJ, 886, 74
Micelotta E. R., Jones A. P., Tielens A. G. G. M., 2010, A&A, 510, A37
Naab T., Ostriker J. P., 2017, ARA&A, 55, 59
Noon K. A., Krumholz M. R., Di Teodoro E. M., McClure-Griffiths N. M., Lockman F. J., Armillotta L., 2023, MNRAS, 524, 1258
Peeters E. et al., 2024, A&A, 685, A74
Pillepich A. et al., 2018, MNRAS, 473, 4077
Rathjen T.-E. et al., 2021, MNRAS, 504, 1039
Rest A., Pierel J., Correnti M., Canipe A., Hilbert B., Engesser M., Sunnquist B., Fox O., 2023, arminrest/jhat: The JWST HST Alignment Tool (JHAT). (Version v2) Zenodo. Available at: https://doi.org/10.5281/zenodo.7892935
Richie H. M., Schneider E. E., Abruzzo M. W., Torrey P., 2024, ApJ, 974, 81
Rupke D., 2018, Galaxies, 6, 138
Sandstrom K. M. et al., 2023, ApJ, 944, L7
Scannapieco E., Brüggen M., 2015, ApJ, 805, 158
Schinnerer E., Leroy A. K., 2024, ARA&A, 62, 369
Schneider E. E., Robertson B. E., 2017, ApJ, 834, 144
Shapiro P. R., Field G. B., 1976, ApJ, 205, 762
Shopbell P. L., Bland-Hawthorn J., 1998, ApJ, 493, 129
Sparre M., Pfrommer C., Ehlert K., 2020, MNRAS, 499, 4261
Strickland D. K., Heckman T. M., 2009, ApJ, 697, 2030
Tan B., Fielding D. B., 2024, MNRAS, 527, 9683
Tan B., Oh S. P., Gronke M., 2021, MNRAS, 502, 3179
Tumlinson J., Peeples M. S., Werk J. K., 2017, ARA&A, 55, 389
Veilleux S., Cecil G., Bland-Hawthorn J., 2005, ARA&A, 43, 769
Veilleux S., Maiolino R., Bolatto A. D., Aalto S., 2020, A&AR, 28, 2
Walter F., Weiss A., Scoville N., 2002, ApJ, 580, L21
Westmoquette M. S., Smith L. J., Gallagher J. S., Walter F., 2013, MNRAS, 428, 1743
Wills K. A., Redman M. P., Muxlow T. W. B., Pedlar A., 1999, MNRAS, 309, 395
Xu X. et al., 2023a, ApJ, 948, 28
Xu X., Heckman T., Yoshida M., Henry A., Ohyama Y., 2023b, ApJ, 956, 142
Zhang M., Li M., 2024, MNRAS, 527, 3418

[1]*Centre for Astrophysics and Supercomputing, Swinburne University of Technology, Hawthorn, VIC 3122, Australia*
[2]*ARC Centre of Excellence for All Sky Astrophysics in 3 Dimensions (ASTRO 3D)*
[3]*Department of Astronomy, University of Maryland, College Park, MD 20742, USA*
[4]*Joint Space-Science Institute, University of Maryland, College Park, MD 20742, USA*
[5]*Department of Astronomy, The University of Texas at Austin, 2515 Speedway, Stop C1400, Austin, TX 78712, USA*
[6]*Center for Computational Astrophysics, Flatiron Institute, 162 5th Ave, New York, NY 10010, USA*
[7]*Department of Astronomy, Cornell University, Ithaca, NY 14853, USA*
[8]*Steward Observatory, University of Arizona, Tucson, AZ 85721, USA*
[9]*Space Telescope Science Institute, 3700 San Martin Drive, Baltimore, MD 21218, USA*
[10]*Department of Astronomy, The Ohio State University, Columbus, OH 43210, USA*

[11]*Center for Cosmology and Astro-Particle Physics, The Ohio State University, Columbus, OH 43210, USA*
[12]*Ritter Astrophysical Research Center, University of Toledo, Toledo, OH 43606, USA*
[13]*Leiden Observatory, Leiden University, PO Box 9513, NL-2300 RA Leiden, the Netherlands*
[14]*European Space Agency, c/o STScI, 3700 San Martin Drive, Baltimore, MD 21218, USA*
[15]*Max-Planck-Institut für Astronomie, Königstuhl 17, D-69120 Heidelberg, Germany*
[16]*Jet Propulsion Laboratory, California Institute of Technology, 4800 Oak Grove Dr., Pasadena, CA 91109, USA*
[17]*Zentrum für Astronomie, Institut für Theoretische Astrophysik, Universität Heidelberg, Albert-Ueberle-Str. 2, D-69120 Heidelberg, Germany*
[18]*Departamento de Astronomía, Universidad de Concepción, Barrio Universitario, Concepción, Chile*
[19]*Instituto Nacional de Astrofísica, Óptica y Electrónica, Luis Enrique Erro 1, Tonantzintla 72840, Puebla, Mexico*
[20]*IPAC, California Institute of Technology, 1200 East California Boulevard, Pasadena, CA 91125, USA*
[21]*Department of Physics & Astronomy, University of Wyoming, Laramie, WY 82071, USA*
[22]*Collège de France, 11 Pl. Marcelin Berthelot, F-75231 Paris, France*
[23]*Observatoire de Paris, 61 avenue de l'Observatoire, F-75014 Paris, France*
[24]*Dept. Física Teórica y del Cosmos, Universidad de Granada, Granada CP 1807, Spain*
[25]*Sterrenkundig Observatorium, Ghent University, Krijgslaan 281-S9, B-9000 Gent, Belgium*
[26]*Department of Physics and Astronomy, University of Kansas, 1251 Wescoe Hall Dr., Lawrence, KS 66045, USA*
[27]*New Mexico Institute of Mining and Technology, 801 Leroy Place, Socorro, NM 87801, USA*
[28]*National Radio Astronomy Observatory, PO Box O, 1003 Lopezville Road, Socorro, NM 87801, USA*
[29]*Millenium Nucleus for Galaxies , Chile*
[30]*Interdisziplinäres Zentrum für Wissenschaftliches Rechnen, Universität Heidelberg, Im Neuenheimer Feld 205, D-69120 Heidelberg, Germany*

This paper has been typeset from a TEX/LATEX file prepared by the author.